Lattice normal modes and electronic properties of the correlated metal $LaNiO_3$

Gaoyang Gou,[1,*] Ilya Grinberg,[1,†] Andrew M. Rappe,[1,‡] and James M. Rondinelli[2,3,§]

[1]*The Makineni Theoretical Laboratories, Department of Chemistry, University of Pennsylvania, Philadelphia, Pennsylvania 19104-6323, USA*

[2]*Department of Materials Science & Engineering, Drexel University, Philadelphia, Pennsylvania 19104, USA*

[3]*X-Ray Science Division, Argonne National Laboratory, Argonne, Illinois 60439, USA*

(Received 30 April 2011; revised manuscript received 9 August 2011; published 3 October 2011)

We use density functional theory calculations to study the lattice vibrations and electronic properties of the correlated metal $LaNiO_3$. To characterize the rhombohedral-to-cubic structural phase transition of perovskite $LaNiO_3$, we examine the evolution of the Raman-active phonon modes with temperature. We find that the A_{1g} Raman mode, whose frequency is sensitive to the electronic band structure, is a useful signature to characterize the octahedral rotations in rhombohedral $LaNiO_3$. We also study the importance of electron-electron correlation effects on the electronic structure with two approaches that go beyond the conventional band theory [local spin density approximation (LSDA)]: the local spin density + Hubbard U method (LSDA + U) and hybrid exchange-correlation density functionals that include portions of exact Fock exchange. We find that the conventional LSDA accurately reproduces the delocalized nature of the valence states in $LaNiO_3$ and gives the best agreement with the available experimental data on the electronic structure of $LaNiO_3$. Based on our calculations, we show that the electronic screening effect from the delocalized Ni $3d$ and O-$2p$ states mitigates the electronic correlations of the d^7 Ni cations, making $LaNiO_3$ a weakly correlated metal.

DOI: 10.1103/PhysRevB.84.144101 PACS number(s): 71.15.Dx, 63.20.dk, 78.30.Er, 79.60.Bm

I. INTRODUCTION

Conducting electrode materials are critical elements in the design of ultrathin ferroelectric devices,[1–4] magnetoresistive elements,[5] and magnetoelectric multiferroic memories.[6] The performance of perovskite-based heterostructures is intimately related to the electronic and atomic coherency across the electrode-oxide interface.[7] For this reason, suitable metallic perovskite oxides that are structurally compatible with the active functional layers are highly desirable. $LaNiO_3$ (LNO) has found widespread use in this capacity,[8–10] because it is a $3d$ transition-metal (TM) oxide that shows no metal-insulator or spin-state transitions.[11,12] At present, it is also actively being pursued as the *functional* oxide component in devices that could harness an electric-field tunable Mott insulator transition (so-called "Mottronic" applications),[13–15] because it is the end member of the rare-earth nickelate series—compounds with small charge-transfer gaps that are highly susceptible to temperature-[16] and pressure-induced[17,18] electronic phase transitions.

Metallicity and magnetism in $3d$ TM oxides are strongly dependent on the valence bandwidth, which originates from the hybridization between the TM $3d$ and the O $2p$ orbitals.[11] In perovskite oxides like LNO, the hybridization derives from the structural connectivity of the NiO_6 octahedral units throughout the crystal. Small changes in the Ni–O–Ni bond angles and the Ni–O bond lengths, therefore, can dramatically alter the electronic properties. For example, a tunable insulator-metal (IM) transition is obtained from the isovalent substitution[19] of La with rare-earth elements: the charge-transfer gap closes, and the IM transition becomes accessible above room temperature as the rare-earth ionic radius increases and straightens the Ni–O–Ni bond angle.

In addition to changes in the structural degrees of freedom, the small spatial extent of the $3d$ orbitals also reduces the valence bandwidth. This sufficiently enhances electron-electron correlation effects such that conventional band metals are often rendered insulating.[20] In $LaNiO_3$, however, the strong Ni $3d$–O $2p$ covalent interactions—formally it contains Ni^{3+} cations in a low-spin $3d^7$ configuration ($t_{2g}^6 e_g^1$)—are anticipated to reduce the correlation effects.[21] Nonetheless, there are clear signatures indicative of important electron-electron interactions in the T^2 dependence of the resistivity and heat capacity measurements.[11,22] Magnetic susceptibility data also reveal enhanced Pauli paramagnetism and effective carrier masses.[16,23–26] Consistent with those studies, temperature-dependent x-ray photoemission finds that the spectral weight of the Ni e_g band at the Fermi level increases upon cooling.[27] A fundamental question regarding the intrinsic properties of $LaNiO_3$ therefore still remains: Which factors of the inter-woven (correlated) electronic and atomic structure support its metallic state?

In this work, we perform first-principles density functional theory (DFT) calculations to investigate how hybridization between the Ni $3d$ and O $2p$ states and the structurally correlated NiO_6 octahedral framework responds to electron-electron interactions. We first examine the temperature-dependent rhombohedral-to-cubic structural phase transition using a Landau formalism[28] and *ab initio*-derived phenomenological coefficients obtained from the conventional band theory [local spin density approximation (LSDA)]. In the rhombohedral phase, we compute the evolution of the Raman-active phonon modes with temperature and find that the LSDA results give good agreement with experiment. We then show how the A_{1g} Raman mode, which describes the rotation of adjacent NiO_6 octahedra, can be used as a structural indicator for the low-temperature rhombohedral phase.

To study the coupling between the lattice modes and the electronic structure, we compare conventional LSDA results with three other approaches designed to improve accuracy: the LSDA + Hubbard U (LSDA + U) method and two hybrid exchange-correlation (XC) functionals, PBE0[29,30] and HSE,[31,32] which contain mixtures of Fock exchange

added to the generalized gradient corrected DFT functional of Perdew, Burke, and Ernzerhof (PBE).[33] We then examine the electronic structure of $LaNiO_3$ by comparing the results obtained from the various functionals with the experimental photoemission spectroscopy (PES) and x-ray photoelectron spectroscopy (XPS) data. We find that the screening effects originating from the hybridized O $2p$ and Ni $3d$ electrons are sufficiently strong that they reduce the electronic correlations in $LaNiO_3$, making it a weakly correlated metal.

II. CRYSTAL STRUCTURE AND RAMAN MODES

The crystallographic tolerance factor[34] for $LaNiO_3$ is $t = 0.97$ and indicates that the aristotype cubic phase is susceptible to octahedral rotations because of an underbonded La-O coordination.[24] Under ambient conditions, bulk $LaNiO_3$ crystallizes in a rhombohedral structure with space group $R\bar{3}c$ [Fig. 1(a)] and is related to the cubic perovskite through a trigonal lattice distortion along the [111]-body diagonal that doubles the primitive unit cell.[11] It also exhibits octahedral rotations, which are equal in magnitude and alternate in sign about each Cartesian direction; this tilt system is classified according to Glazer notation[35,36] as $a^-a^-a^-$ [Fig. 1(b)]. Similar to other rhombohedrally distorted perovskites,[37] $LaNiO_3$ undergoes a temperature-induced rhombohedral-to-cubic phase transition[38] upon heating: the NiO_6 octahedral rotation angle θ decreases continuously to 0° as it approaches the cubic phase.

In the $R\bar{3}c$ space group, the La cations occupy the $2a$ $(\frac{1}{4},\frac{1}{4},\frac{1}{4})$ Wyckoff positions, while the Ni cations occupy the $2b$ $(0,0,0)$ positions. The oxygen atoms are at the $6e$ $(x,\bar{x}+\frac{1}{2},\frac{1}{4})$ site, where x is the only free internal structural parameter that sets the rotation angle of the NiO_6 octahedra. These 10 atoms in the primitive rhombohedral unit cell give rise to 30 zone-center vibrational modes with the irreducible representations (irreps)

$$\Gamma = A_{1g} + 3A_{2g} + 4E_g + 2A_{1u} + 4A_{2u} + 6E_u,$$

where the E_g and E_u modes are two-dimensional (2D) irreps. The infrared-active and acoustic modes transform as $4A_{2u} + 6E_u$, while the Raman-active modes are given as $A_{1g} + 4E_g$.

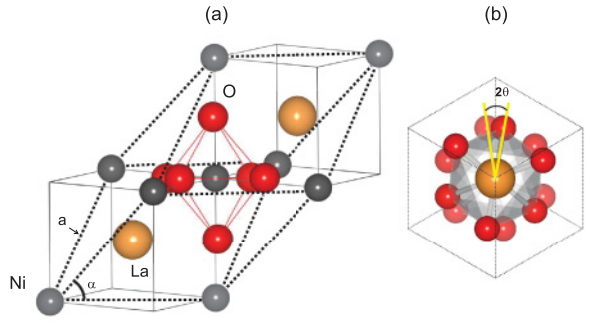

FIG. 1. (Color online) (a) The crystal structure of rhombohedral $R\bar{3}c$ $LaNiO_3$ possesses antiphase rotations ($a^-a^-a^-$ tilt system) of adjacent NiO_6 octahedra with angle θ (b) about the [111] trigonal axis. The relationship between the pseudocubic perovskite cell (solid lines) and the rhombohedral lattice vectors (dashed lines) of length a is also illustrated.

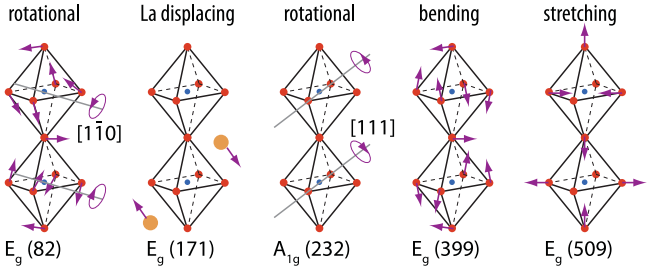

FIG. 2. (Color online) Displacement patterns for the Raman-active lattice normal modes in the $R\bar{3}c$ structure. The corresponding symmetry labels and our calculated LSDA frequencies (in cm^{-1}) are given for reference.

The A_{1g} and E_g Raman modes of the rhombohedral structure are mainly related to collective modes of the oxygen octahedral network (Fig. 2): the A_{1g} mode describes the rotations of the NiO_6 about the trigonal [111] axis, and the E_g modes describe antiparallel La displacements, Ni–O bond bending, stretching, and octahedral rotations about axes perpendicular to the [111] direction.

III. THEORETICAL METHODS

A. LSDA

We use two DFT implementations in this study, the QUANTUM ESPRESSO code (QE)[39] and the Vienna *ab initio* Simulation Package (VASP).[40,41] Our reference electronic structure model to which we compare our advanced treatments of correlation effects is the frequently used LSDA XC functional.[42] Both DFT codes use the Perdew-Zunger parametrization[42] of the Ceperley-Alder data[43] for the XC functional. In all calculations, we constrain a collinear spin configuration for Ni ions. The atomic positions in the rhombohedral structure are optimized by starting from the positions reported in Ref. 11, and the ionic coordinates are relaxed until the Hellmann-Feynman forces on the atoms are less than 0.1 meV $Å^{-1}$.

1. VASP *details*

We treat the core and valence electrons for all calculations in VASP using the projector augmented wave method[44] with the valence electron configurations $5p^65d^16s^2$ (La), $3p^63d^94s^1$ (Ni), and $2s^22p^4$ (O) and a 650-eV plane-wave cutoff. We use a Gaussian smearing of 0.05 eV over a $7 \times 7 \times 7$ Monkhorst-Pack k-point mesh[45] centered at Γ for the Brillouin zone (BZ) integrations (172 points are sampled in the irreducible BZ) in the 10-atom rhombohedral unit cell.

We obtain the phonon frequencies at the Γ point by calculating total energies with respect to atomic displacements from the reference $R\bar{3}c$ structure. In this frozen-phonon method, a series of small (symmetry-inequivalent) atomic displacements is imposed along different Cartesian directions. We calculate the dynamical matrix from the Hellmann-Feynman forces[46] induced on the ions after making small positive and negative displacements (to remove any quadratic effects) about the reference structure positions from the total energy DFT calculation. Diagonalization of the dynamical matrix yields the atomic displacement patterns (eigenvectors) and phonon mode frequencies (eigenvalues).

TABLE I. Structural parameters obtained for $R\bar{3}c$ $LaNiO_3$ within the LSDA from the two codes used in this work and their comparison with experimental data (cf. Ref. 11). In the rhombohedral setting, the rotation angle of adjacent NiO_6 octahedra along the trigonal axis is given as $\theta = \arctan(2\sqrt{3}u)$, where $x = u + \frac{3}{4}$.

		Theory	
	Experiment	VASP	QE
x	0.7968	0.787	0.801
a (Å)	5.3837	5.303	5.324
α_{rho} (°)	60.8596	60.72	61.39
d(Ni–O) (Å)	1.933	1.896	1.923
∠Ni–O–Ni (°)	164.8	167.9	163.3
θ NiO_6 rotation (°)	9.2	7.35	10.08
Ω (Å^3/f.u.)	56.2386	53.57	55.03

2. QE details

In our plane-wave calculations with the QE code, we use norm-conserving optimized[47] designed nonlocal[48] pseudopotentials. The following valence electron configurations are used: $5s^2 5p^6 4f^0 5d^0 6s^0 6p^0$ (La), $3d^9 4s^1 4p^0$ (Ni), and $2s^2 2p^4$ (O). Note that in both VASP and QE, partial core corrections are included in the Ni pseudopotentials following the prescription in Ref. 49.

We sample the BZ using an $8 \times 8 \times 8$ Monkhorst-Pack k-point mesh. A plane-wave energy cutoff of 50 Ry is used for calculation. Good convergence is reached, as test calculations with a higher energy cutoff (up to 75 Ry) yield the same results. We obtain phonon modes and displacement vectors using density functional perturbation theory,[50,51] by constructing the interatomic force constants from the dynamical matrices obtained on a uniform $4 \times 4 \times 4$ q-point grid. The phonon frequencies and vibrational eigenvectors at arbitrary q vectors are then calculated from diagonalization of the dynamical matrix.

We point out here that both implementations of the DFT at the LSDA level give good structural agreement (Table I). This fact is important for the comparison study we make later, which uses various functionals available in the different codes. Each code yields a small underestimation of the experimental lattice constant which is typical for the LSDA. The QE code more closely reproduces the experimentally measured Ni–O–Ni rotation angles, whereas the VASP code gives a better rhombohedral angle (α_{rho}). For the electronic and magnetic structure of LNO, both codes predict LNO as a nonmagnetic metal, which is the reasonable representation of the experimentally observed Pauli paramagnetic ground state.[24] Detailed electronic properties for LNO are presented in Sec. IV. Here we note that a partial core correction for Ni is crucial to obtain the correct ground state of paramagnetic LNO. Without partial core corrections, LSDA calculations yield a spin-polarized solution with a nonzero local magnetic moment on the Ni cations.

B. LSDA + U

A complete description of correlated $3d$ TM oxides with narrow valence bandwidths is challenging within a density functional approach due to the limitations of standard XC potentials in describing localized electronic states. To remedy this problem, we use "beyond-LSDA" techniques, starting with the LSDA + U approach. This method is generally regarded to be the most computationally feasible means to reproduce the correct ground states in correlated systems.[52] In this formalism, the LSDA energy functional is expanded to include an additional on-site orbital-dependent energy term cast as a Hubbard repulsion U and an intratomic Hund's exchange energy J.

To reduce the ambiguity in the definition of the LSDA + U parameters, we use the spherically averaged form of the rotationally invariant LSDA + U method[52] introduced by Dudarev *et al.*,[53] with only one effective Hubbard term, $U_{\text{eff}} = U - J$. We treat the double-counting term within the fully localized limit.[54]

The change in total energy E_U upon including the Hubbard correction to the XC potential is

$$E_U(J=0) = \frac{U_{\text{eff}}}{2} \sum_i \sum_{m\sigma} n^i_{m\sigma}\left(1 - n^i_{m\sigma}\right), \tag{1}$$

where $n^i_{m\sigma}$ are the spin (σ) and orbital (m) occupation numbers at site i. In the limit where the occupation matrices are integer and diagonal, the LSDA + U correction can be understood as a shift in the occupied orbitals ($n_m = 1$) by $-U/2$ to lower energy and by $+U/2$ higher in energy for unoccupied orbitals ($n_m = 0$).

In this study we examine U_{eff} values of 0, 3 and 6 eV for the correlated Ni $3d$ orbitals states; the standard LSDA corresponds to a $U_{\text{eff}} = 0$ eV. We note that throughout the remainder of the paper, U denotes the effective Hubbard parameter. We discuss the structural changes induced by varying U in the subsequent sections.

1. Self-consistent Hubbard U

We also calculate a self-consistent U parameter for $LaNiO_3$ following the scheme developed by Cococcioni and de Gironcoli.[55] Their approach relies on the fact that the potential U restores the correct piecewise linear behavior of the system's total energy as a function of electron number, whereas the LSDA functional incorrectly predicts parabolic dependence of energy on occupation number. The effective interaction parameter U is deduced from Janak's theorem and linear response theory as

$$U = \left(\chi_0^{-1} - \chi^{-1}\right)_{ii} \quad \text{with} \quad \chi_{ij} = \frac{dn^i}{d\alpha_j}. \tag{2}$$

Here n^i is the occupation number of the localized levels at site i and α_j represents the potential shift applied on the localized orbital at site j. The response matrix χ_0 describes the noninteracting contribution to the band structure after application of a potential shift α, while χ represents the fully self-consistent response to the same potential shift. In practice, the first term χ_0 is computed from the first iteration in the self-consistent electronic minimization.

We compute the linear response of the occupation number n^i using the LSDA functional and norm-conserving pseudopotentials within the QE package. The full response matrices χ_0 and χ are then computed by performing the linear response calculation within a $2 \times 2 \times 2$ pseudocubic supercell (40-atom

cell, containing 8 Ni atoms), which is large enough to give a converged U value and avoid spurious interactions from the local potential α on neighboring Ni sites.

The low-spin Ni $3d$ orbital occupation anisotropy—a fully filled t_{2g} manifold and a quarter-filled e_g shell—suggests that the effective Coulomb repulsion experienced by an electron on different orbitals should also be substantially different.[56] For this reason, we further decompose the orbital occupancy $n^i \rightarrow n^i_m$ (m is the angular momentum quantum number, and orbital occupation n^i_m here refers to a Löwdin atomic charge) into crystal-field split d-manifold contributions by projecting the valence states $|\Psi^\sigma_{kv}\rangle$ onto atom-centered sites i with a Löwdin orthogonal atomic basis set $|\phi^i_m\rangle$ as

$$V_U|\Psi^\sigma_{kv}\rangle = \frac{U}{2}\sum_i\sum_{m\sigma}\left(1-2n^i_{m\sigma}\right)|\phi^i_m\rangle\langle\phi^i_m|\Psi^\sigma_{kv}\rangle. \quad (3)$$

By replacing the orbital occupancy n^i in Eq. (2) with n^i_m, we can calculate the effective Hubbard term U for the two independent Ni d manifolds: $U(e_g)$ and $U(t_{2g})$, respectively. Since the t_{2g} manifold is fully occupied [$n(t_{2g}) \approx 1$], the linear response calculation of $U(t_{2g})$ requires that the contribution from these states to the total Coulomb interaction be nearly 0. Within the numerical noise of our calculations we find this to be the case. Figure 3 shows that the difference in the χ_0 and χ response functions (slopes) of the t_{2g} states is practically negligible. The Ni e_g states, however, which are partially filled, have a substantial non-zero interaction, $U(e_g)$. These states lead to a self-consistent Hubbard U value of 5.74 eV for $LaNiO_3$.

Recently Nohara *et al.* studied $LaNiO_3$ with LSDA + U and GW methods[57] and fitted their calculated energy spectra to experimental XPS and x-ray adsorption spectroscopy (XAS) data[58] to obtain a Coulomb interaction of $U = 7.0$ eV and an exchange interaction $J = 1.3$ eV for the Ni d manifold. These values correspond to an effective Hubbard U term ($U_{\text{eff}} = 5.7$ eV) which is consistent with our linear-response calculation of U.

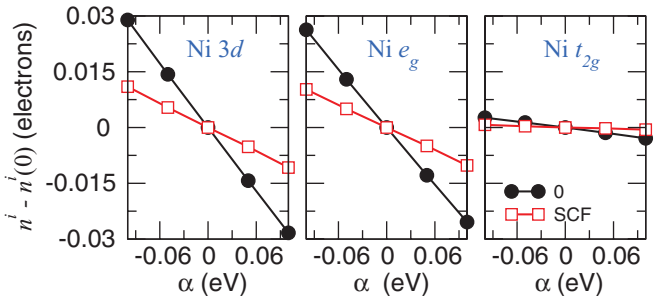

FIG. 3. (Color online) Occupation numbers n^i for the total Ni $3d$, e_g, and t_{2g} orbitals in $LaNiO_3$, with respect to potential shift α for the initial (0) (filled circles) and self-consistent (open squares) electronic configurations. The slopes of the linear data fits are used to construct the χ_0 and χ response matrices. Occupation numbers are normalized by subtracting the occupation values $n_i(0)$ with a zero potential shift ($\alpha = 0$).

C. Hybrid functionals

Recent studies[31–33,59] have demonstrated that local or gradient-corrected density functionals for exchange do not closely reproduce Hartree-Fock calculations, and that inclusion of some exact Fock exchange improves electronic structure properties including band gaps, orbital localization, and electronic polarizations.[60] Accordingly, in the present work, we use the PBE0 and HSE hybrid functionals as implemented in the QE package and then contrast them with the LSDA.

The exchange terms (V_x) in the PBE0 functional are constructed by mixing 25% of exact exchange with 75% GGA-PBE exchange,[29] while the electron correlation (V_c) part is represented using only the correlation components from the PBE functional:[33]

$$V^{\text{PBE0}}_{xc} = \tfrac{1}{4}V_x + \tfrac{3}{4}V^{\text{PBE}}_x + V^{\text{PBE}}_c. \quad (4)$$

The one-quarter mixing parameter of exact exchange in the PBE0 functional was obtained by fitting to the atomization energies of a large database of molecules.[29] For periodic bulk systems, however, it is argued that the best fraction of exact exchange for modeling solid-state electronic structure is highly system dependent.[29,61]

The HSE hybrid functional[31,32] is less computationally demanding than the PBE0 (unless the recent Wannier function implementation described in Ref. 30 is used), since it avoids the slowly decaying Fock-exchange interactions by replacing the long-range part of the Coulomb-kernel with a density functional. This approximation makes the HSE functional more efficient for plane-wave calculations of periodic systems. The expression for the XC potential is given as

$$V^{\text{HSE}}_{xc} = \tfrac{1}{4}V^{\text{sr},\mu}_x + \tfrac{3}{4}V^{\text{PBE,sr},\mu}_x + V^{\text{PBE,lr},\mu}_x + V^{\text{PBE}}_c, \quad (5)$$

where μ is the parameter that controls the decomposition of the Coulomb kernel into short-range (sr) and long-range (lr) exchange contributions. This type of screened exact exchange is absent in the PBE0 functional. In this work, we follow the HSE03 parametrization,[31] which sets the cutoff parameter to $\mu = 0.109$ Å^{-1}.

Similarly to PBE0, the Fock-mixing parameter in HSE varies approximately in proportion to the inverse static dielectric constant (ε^{-1}_∞) and, therefore, also becomes highly system dependent. For metals with excellent screening, ε^{-1}_∞ approaches 0. Therefore PBE0 or HSE calculations which incorporate some Fock exchange may lead to severe overestimation in orbital bandwidths and spin-exchange splitting parameters for such materials.[62]

In our hybrid functional calculations on metallic $LaNiO_3$, we use a dense BZ sampling ($8 \times 8 \times 8$ k-point grid) for accurate evaluation of the Fock-exchange operator in reciprocal space.[62] Due to the heavy computational cost, we are unable to perform the structural optimization for LNO using the hybrid functionals in the present work. According to our test calculations using the LSDA, PBE, and LSDA + U functionals, the subtle differences between the ground-state atomic positions produce negligible changes to the computed electronic band structure. We therefore choose the LSDA optimized atomic structure as the ground-state structure for use in the hybrid functional calculations.

IV. RESULTS AND DISCUSSION

In this section, we present our first-principles results on the structural, vibrational, and electronic properties of bulk $LaNiO_3$ obtained using the various XC functionals. This section is organized as follows: we first investigate the structural phase transition and temperature-dependent Raman phonon modes of $LaNiO_3$ using the conventional LSDA. We then examine how the atomic structure, Raman phonon modes, and electronic properties of $LaNiO_3$ are modified with various treatments of electron-electron correlation effects. Finally, by comparing the density-of-states (DOS) results obtained from the different functionals to the experimental spectroscopic data, we identify which XC functional best reproduces the intrinsic electronic properties of $LaNiO_3$.

A. Structural phase transition

The temperature-induced rhombohedral-to-cubic phase transition in $LaNiO_3$ manifests as a cooperative rotation of NiO_6 octahedra along the trigonal lattice axis.[63] In this section, we show how the structural transition to the rhombohedrally distorted perovskite phase is characterized by a specific soft mode which has a frequency that collapses to zero as the system approaches the cubic phase.[37] We note that all results in this section are obtained with the LSDA XC functional and norm-conserving pseudopotentials as implemented in the QE.

1. Minimal Landau model

In the Landau theory framework for phase transitions, the free energy of the system is expanded in powers of an order parameter that characterizes the transition. From our previous discussion of the low-temperature $R\bar{3}c$ crystal structure of $LaNiO_3$, the only free *internal* parameter is the oxygen position x at the 6*e* Wyckoff site. Therefore, the natural order parameter to characterize the rhombohedral-to-cubic phase transition is a structure-adapted form of the free Wyckoff position: the NiO_6 octahedra rotation angle θ (Fig. 1).

We expand the free energy G in even powers (up to fourth order) of this rotation angle order parameter θ as

$$G(\theta,T) = G_0(T) + \kappa(T - T_C)\theta^2 + \lambda\theta^4, \tag{6}$$

where κ and λ are temperature-independent coefficients and θ is the angle of rotation about the [111] direction. We next "freeze in" the NiO_6 rotation pattern [inset in Fig. 5(b)], which corresponds to the A_{1g} Raman mode of the $R\bar{3}c$ phase. In Fig. 4, we show our calculated values of the total energy versus NiO_6 rotation angle θ computed at the LSDA equilibrium volume. Our fit of the data to Eq. (6) yields excellent agreement and approximately corresponds to the free energy at zero temperature $G(\theta, T = 0\ \text{K})$. From the minimum of the free energy $(\partial G/\partial\theta)_T = 0$, we obtain the T dependence of θ,

$$\theta^2 = \frac{\kappa}{2\lambda}(T_C - T) \quad \text{for} \quad T < T_C, \tag{7}$$

and a critical rotation angle at $T = 0$ K of $\theta_C = 10.08^\circ$ (the optimized θ from the LSDA calculation).

We next calculate the energy stabilization obtained from freezing-in the NiO_6 rotation at 0 K as the difference between the cubic and the rhombohedral phases, $\Delta E = 177$ meV/10-atom unit cell, given by the well depth from the total energy

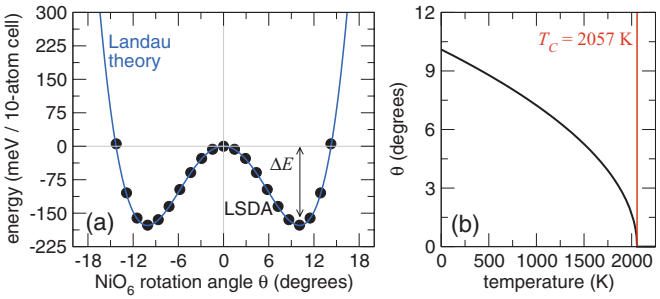

FIG. 4. (Color online) (a) Landau free energy $G(\theta, T = 0\ \text{K})$ of $LaNiO_3$ as a function of the order parameter θ. Solid lines are calculated using Landau theory, and filled symbols correspond to LSDA total energy results. (b) Equilibrium order parameter θ as a function of temperature; the second-order phase transition occurs at $T = T_C$.

calculations [Fig. 4(a)]. With increasing temperature, the energy stabilization from the structural distortion decreases until, at $T = T_C$, the thermal excitation energy is equivalent to ΔE and the double-well potential becomes a single well with one minimum at $\theta = 0^\circ$. With these conditions, we write

$$\Delta E = (T \cdot \Delta S)_{T=T_C}, \tag{8}$$

where ΔS refers to the entropy difference between the cubic and the rhombohedral phases. Since $LaNiO_3$ has a Debye temperature Θ_D of 420 K[22], at the structural transition $T = T_C$, $T_C \gg \Theta_D$, we are able to confidently treat each lattice mode as an independent harmonic oscillator which subsequently contributes Nk_BT to the free energy.

For the 10-atom rhombohedral $LaNiO_3$ unit cell, a single soft mode $(N = 1)$ describes the transition from the high-temperature cubic phase; therefore, $\Delta S \simeq k_B$. From these conditions, we calculate the LSDA critical temperature for the structural phase transition T_C to be 2057 K, which is close to the experimental[63] result ($T_C = 1780$ K). The overestimation of T_C likely originates from the calculated enhancement of θ_C, which increases the energy difference between the cubic and the rhombohedral phases.

Using this calculated T_C value, and combining with our earlier calculated DFT total energy results, we obtain the coefficients in Eq. (6) $\kappa = 1.696\ \mu\text{eV/K}\cdot(\text{deg})^2$ and $\lambda = 17.1\ \mu\text{eV/(deg)}^4$. These values combined with Eq. (7) give the second-order temperature dependence of the NiO_6 octahedral rotational angle $\theta(T)$ shown in Fig. 4(b).

2. Correlation of volume expansion with phase transition

With increasing temperature, the $LaNiO_3$ lattice undergoes a thermal volumetric expansion process. To precisely simulate the temperature-induced rhombohedral-to-cubic phase transition process, it is necessary to evaluate the effect of volume expansion on the NiO_6 octahedral rotations across the structural phase transition.

By including the coupling between the order parameter θ and the equilibrium atomic volume V, we extend the minimal 1D Landau model discussed in the previous subsection into a 2D case, with the free energy G given as

$$G(\theta,V,T) = G_0(V,T) + \kappa(V)(T - T_C)\theta^2 + \lambda(V)\theta^4, \tag{9}$$

where V is the equilibrium $LaNiO_3$ volume at a given temperature, and the coefficients κ and λ are expressed as a function of V. From 0 K to room temperature, we assume a linear volumetric thermal expansion, $V(T) = V_0 \times (1 + \alpha_V T)$, where V_0 is the volume at 0 K and the thermal volumetric expansion coefficient $\alpha_V = 1.624 \times 10^{-5}/\mathrm{K}$ is from experiment.[63]

To correlate the DFT total energy results with the Landau free energy at 0 K, we rewrite Eq. (9) as

$$G(\theta, V, T = 0K) = G_0(V) + A(V)\theta^2 + B(V)\theta^4. \quad (10)$$

This form indicates a practical route to calculate the optimal NiO_6 rotation angle θ_C with respect to V. We apply the procedure described in the previous subsection but now obtain volume-dependent coefficients A and B by fitting each coefficient through a Taylor expansion about the equilibrium volume:

$$\begin{aligned} A(V) &= A_0 + A_1\left(\frac{\Delta V}{V_0}\right) + A_2\left(\frac{\Delta V}{V_0}\right)^2 + \cdots, \\ B(V) &= B_0 + B_1\left(\frac{\Delta V}{V_0}\right) + B_2\left(\frac{\Delta V}{V_0}\right)^2 + \cdots, \end{aligned} \quad (11)$$

where $\Delta V = V - V_0$. With this method, we obtain the following coefficients: $A_0 = -3.6$, $A_1 = -16.6$, and $A_2 = 1600.1$ meV/(deg)^2 and $B_0 = 17.9$, $B_1 = -15.5$, and $B_2 = -1664.0$ μeV/(deg)^4.

This treatment of changes in the lattice volume at the rhombohedral-to-cubic transition reveals that the magnitude of our phenomenological coefficients A (B) increase (decrease) with increasing cell volume. Thus, the curvature of the double-well potential (Fig. 4) becomes steeper and its depth deeper as the cell volume increases; this fact indicates that the thermal expansion effect will hinder the rhombohedral-to-cubic phase transition in $LaNiO_3$. Nonetheless, the extent of the thermal volumetric expansion effect is very limited, i.e., from 0 K to room temperature, $\Delta V/V_0 \simeq 0.5\%$, which leads to changes in the coefficients A and B by less than 1% and a deviation in our simulated rotation angle θ at 300 K by 0.2° compared to the *volume-independent* model described previously. We conclude that, for the temperature range we investigated (0 K to room temperature), treating the phenomenological coefficient in our Landau theory as volume independent suffices to produce an accurate description of the temperature-induced octahedral phase transition in $LaNiO_3$.

3. *Temperature-dependent Raman frequencies*

We next study the structural and vibrational properties of $LaNiO_3$ at finite temperatures. As the temperature increases the NiO_6 rotation angle θ decreases [Fig. 4(b)] and the Ni–O bond length increases. To capture this effect in our simulation, we choose to combine the cell parameters a and α for $LaNiO_3$ at a given temperature with a specific NiO_6 rotation angle θ and Ni–O bond length [d(Ni–O)]. The rotation angle θ for a given temperature is obtained from Eq. (7), while for d(Ni–O), we refer to the experimental temperature-dependent neutron scattering results.[11] To sample the d(Ni–O)–temperature space at experimental values not available, we assume linear thermal expansion. We then relax only the internal coordinates and use the structures that yield the best experimental agreement to represent a snapshot of the experimental LNO structure.

We use these structures to perform phonon calculations and obtain the temperature-dependent Raman frequencies [Fig. 5(a)]. A comparison of the experimental[63] data to our DFT-calculated temperature-dependent Raman frequencies reveals a good agreement: both data sets show red shifts in the Raman frequencies with increasing temperature. The calculated high-frequency E_g mode, which corresponds to stretching of the Ni–O bonds, however, is systematically underestimated by around 10%. The LSDA also predicts that the frequencies of the bending and stretching E_g modes decrease nearly twice as rapidly as that experimentally observed.

We now connect the frequency of the A_{1g} Raman mode ($\omega_{A_{1g}}$) and the order parameter θ described in the previous subsections. Here, we assign the lattice mode to the stiffness κ, or the curvature (second-order derivative) of the potential well, as

$$\omega^2_{A_{1g}} \propto \frac{\partial^2 G}{\partial \theta^2} = 4\kappa(T_C - T) \quad \text{for} \quad T < T_C. \quad (12)$$

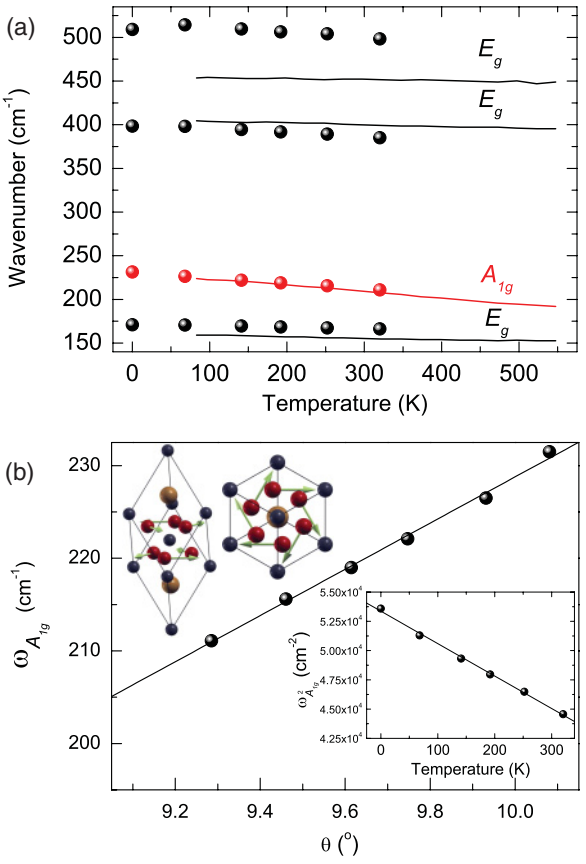

FIG. 5. (Color online) (a) Temperature-dependent Raman frequencies for rhombohedral $LaNiO_3$ structures. Solid lines indicate experimental results taken from Ref. 63. Results from our LSDA calculations are shown as filled circles. (b) We observe linear scaling behavior between the A_{1g} Raman frequency and the NiO_6 octahedral rotation order parameter θ. The fitted solid line is a guide for the eye. Inset at upper left: Vibrational pattern of the A_{1g} mode (both side and top views). Inset at lower right: A linear change in the squared A_{1g} soft-mode frequency with temperature.

By comparing Eq. (7) with Eq. (12), we find that $\omega_{A_{1g}} \propto |\theta|$ and in the temperature limit $T \to T_C$ both θ and $\omega_{A_{1g}}$ approach 0. Using our fitted value of κ, we show in Fig. 5(b) that $\omega_{A_{1g}}$ varies linearly with θ. We also predict from the slope in Fig. 5(b) that the Raman-mode shift due to changes in the NiO_6 rotation angle is $\omega_{A_{1g}}/\theta = 23.0\,\mathrm{cm}^{-1}/\mathrm{deg}$. Finally, we plot the temperature dependence of the squared A_{1g} frequency (Fig. 5, inset) and find that $\omega^2_{A_{1g}}$ decreases linearly with temperature, confirming the $\omega^2_{A_{1g}}(T)$ relation in Eq. (12) . On the basis of these findings, we conclude that the A_{1g} soft mode is an excellent signature for the magnitude of the octahedral rotations in rhombohedral $LaNiO_3$ and its deviation from the cubic phase.

B. Correlation effects on the atomic structure and Raman phonon modes

We focus in this section on how Raman-active mode frequencies are modified through changes in electron-electron correlations. We first decompose the effect of correlation through the Hubbard U term on the structural degrees of freedom by fixing the lattice parameter to that of the experimental $R\bar{3}c$ structure and allowing the internal atomic positions to fully relax. The results of our atomic relaxations for LSDA + U values of 0, 3, and 6 eV are summarized in Table II. In all cases, the LSDA + U functional accurately reproduces the known experimental ground-state structure with the minor caveats we discuss next.

With increasing correlation, we find that the NiO_6 rotation angle increases beginning from the LSDA structural ground state ($U = 0$ eV), which slightly underestimates the rotation angle, to $U = 3$ eV, which overestimates it by approximately 1°. By further increasing the Hubbard U value to 6 eV, we find that the rotation angle decreases. The consequence of keeping the unit cell volume and rhombohedral angle fixed is that the change in the NiO_6 rotation angle must be accommodated by bond stretching (or compression) rather than through rigid rotations (constant Ni–O bond lengths). Because the Ni atoms also occupy the 2*b* Wyckoff position with $\bar{3}$ site symmetry, all Ni–O bond lengths are required to be equivalent. We thus observe that our calculated Ni–O bond lengths respond proportionally to the NiO_6 rotation angle θ (Table II).

We next examine the change in the electronic structure with increasing correlation to evaluate how the electronic states around the Fermi level are modified. We show in Fig. 6 the electronic DOS values as a function of the Hubbard U

TABLE II. Optimized internal structural parameters of $R\bar{3}c$ $LaNiO_3$ at the experimental[11] cell parameter a and rhombohedral angle α, calculated with the LSDA + U functional and projector augmented wave pseudopotentials as implemented in VASP.

		LSDA + U		
	Expt.	$U = 0$ eV	$U = 3$ eV	$U = 6$ eV
x	0.797	0.796	0.800	0.797
d(Ni–O) (Å)	1.933	1.932	1.935	1.933
∠Ni–O–Ni (deg)	164.8	165.2	163.9	164.6
θ NiO_6 rotation (deg)	9.20	8.97	9.77	9.33

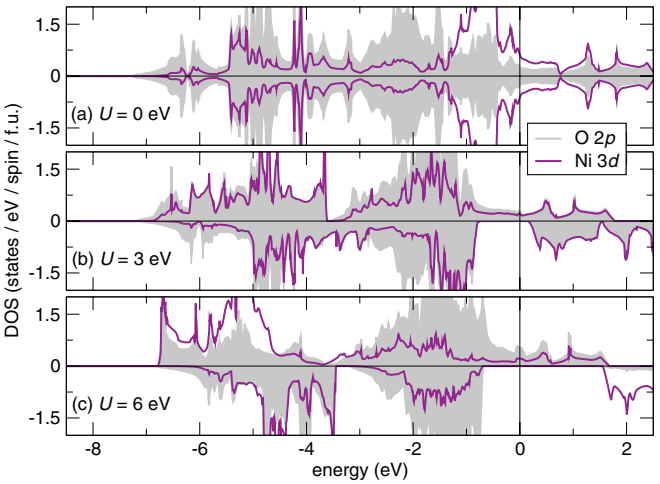

FIG. 6. (Color online) Spin- and atom-resolved densities of states (DOS) for the $LaNiO_3$ structures reported in Table II with the LSDA + U exchange-correlation functional.

value obtained by LSDA + U calculations with the VASP code. Consistent with earlier band structure calculations on bulk $LaNiO_3$ with the LSDA ($U = 0$ eV) functional,[64–66] we find a nonmagnetic ground state with localized Ni 3*d* states centered 1.0 eV below the Fermi level (E_F). A set of delocalized Ni 3*d* states crosses E_F, while the O 2*p* states are distributed throughout the entire valence band.

Here, we apply a Hubbard U term to the Ni d states and anticipate the on-site Coulomb interaction to localize the itinerant Ni d electrons at E_F and stabilize a ferromagnetic spin configuration. Indeed, we find a half-metallic ferromagnetic ground state (1 μ_B/f.u.). Note that this configuration, however, has not been experimentally reported. For $U = 3$ eV, we find that the DOS at the Fermi level is substantially suppressed compared to the LSDA, with the Ni d states shifting to lower energy. Due to the increased rotational angle of the NiO_6, we find that a pseudogap opens in the majority-spin DOS around −3.5 eV with reduced hybridization between the Ni 3*d* and O 2*p* states. With a further increase in the U value [Fig. 6(c)], we find that most of the majority-spin Ni 3*d* electrons are shifted completely to the bottom of the valence band around −5.5 eV. The states at E_F are now mainly of O 2*p* character, with a small contribution from Ni 3*d* electrons.

We now compute the Raman-active lattice modes for the structures listed in Table II to explore the change in Raman frequencies with an increasing Hubbard U value. We begin by comparing the experimentally measured values to our calculated ones (Table III). The best agreement with the experimental data is for the LSDA ($U = 0$ eV) XC functional. A Hubbard U value of 3 eV overestimates the low-frequency Raman mode with E_g symmetry (La antiparallel displacements), while it underestimates the two high-frequency E_g modes (Ni–O bond bending and stretching).

Interestingly, with the LSDA + $U = 6$ eV functional we find an unstable (imaginary) zone-center phonon ($246i$ cm^{-1}) with A_{2g} symmetry, indicating that the rhombohedral structure with the simple $a^-a^-a^-$ tilt pattern is unstable. The atomic displacement pattern of the imaginary mode corresponds to a 3D checkerboard arrangement of dilated and contracted

TABLE III. Raman-active vibrational modes computed using the LSDA + U formalism at the experimental cell volume are compared to measured values. All mode frequencies are given in wavenumbers (cm^{-1}). Experimental values are taken from Ref. 63.

	E_g	E_g	A_{1g}	E_g	E_g
Experimental	–	156	209	399	451
$U = 0$ eV	61.8	155.0	215.4	372.6	451.7
$U = 3$ eV	94.3	164.8	245.5	387.3	413.5
$U = 6$ eV	54.6	156.7	219.4	316.0	381.8

octahedra—the so-called octahedral "breathing" mode that often accompanies charge disproportionation.[67] This structural feature, however, has not been observed in any temperature-dependent x-ray studies on $LaNiO_3$. We therefore suggest that this correlation-induced octahedral distortion is a spurious artifact of using too large an on-site Coulomb repulsion interaction in the LSDA + U calculation. We conclude that a Hubbard U value of less than 6 eV should be used when simulating $LaNiO_3$, because of the overall poor accuracy in the calculated Raman modes (Table III), despite such large Hubbard values closely reproducing the experimental lattice parameters of the $LaNiO_3$ phase (Table II).

We now explore how changes in the electron correlations modify the lattice volume by fully relaxing both the internal atom positions and the rhombohedral structure (Table IV). For the LSDA + U XC potential, we qualitatively find the same structural trends as in Table II. While the LSDA underestimates the atomic volume, when we increase the value of U, the cell volume increases; this can be understood as a result of enhanced electrostatic repulsion.

We also compute the LNO ground-state structures with the LSDA, PBE, and PBEsol functionals and norm-conserving pseudopotentials as implemented in QE. Typically, the LSDA underestimates the lattice constant a, cell volume, and Ni–O bond length, but it closely reproduces the experimentally measured Ni–O_6 octahedral rotation angle θ. For the PBE functional, we find that both the bond length and the octahedral rotation angles are overestimated. On the other hand, the PBEsol gradient-corrected functional corrects some of the above-mentioned overestimation from the PBE; although still slightly overestimating the rotation angle, it does provide the best agreement with the experimental lattice constant a, Ni–O bond length, and equilibrium atomic volume, among all the functionals we used for the structural optimization.

We now use these ground-state structures, listed in Table IV, and calculate their Raman-active mode frequencies to examine the effect of lattice volume on the mode frequencies. Comparing these LSDA + U results (Table V) to our previously calculated lattice modes obtained using the same functionals but at the experimental volume (Table III), we find that the LSDA ($U = 0$ eV) functional provides the best agreement with experimental data. As before, we find an unstable zone-centered NiO_6 octahedral breathing mode in our calculations with $U = 6$ eV. Interestingly, the LDSA + Hubbard U method accurately predicts the ground-state structural properties; however, it also leads to poor predictions for the lattice normal modes. We note that in this case, simply reproducing the correct ground-state atomic structure is not a sufficient criterion to evaluate the performance of a functional. This caveat is important to consider, especially in the first-principles search for perovskite materials with large electron-phonon interactions.

We also find a close relation between the predicted Raman phonon frequencies and the structural parameters of the bulk rhombohedral LNO, especially for the A_{1g} and the two high-frequency E_g modes. Typically, the A_{1g} mode frequency is sensitive to the octahedral rotation angle θ, whereas the bond bending and breathing E_g modes are substantially more sensitive to the predicted Ni–O bond length and cell volume Ω, respectively. The LSDA underestimates both the lattice constant a and the cell volume Ω, but it also overestimates the rhombohedral angle α_{rho}. This leads to a cancellation of errors and an overall good prediction of both θ and d(Ni–O) and, therefore, calculated rotation (A_{1g}) and bending (E_g) phonon frequencies are close to experiment. The LSDA functional only overestimates the stretching E_g-mode frequency (by 10%) due to the underestimation of cell volume.

Compared to the LSDA, the PBEsol functional improves the prediction of the structural parameters, such as a and Ω (Table IV). Except for the overestimation of θ, PBEsol also predicts d(Ni–O) bond lengths close to experiment. Therefore, as reported in Table V, the two high-frequency E_g modes are in good agreement with experiment, but the A_{1g} mode is overestimated by more than 20%. The PBE functional, in contrast, overestimates all of the major bulk LNO structural parameters, thus providing the poorest description of the Raman frequencies among the three functionals explored in

TABLE IV. Fully optimized structural parameters of $R\bar{3}c$ $LaNiO_3$ (rhombohedral setting), calculated from the various exchange-correlation functionals.

		VASP: LSDA + U			QE		
	Expt.	$U = 0$ eV	$U = 3$ eV	$U = 6$ eV	LSDA	GGA-PBE	PBEsol
x	0.7968	0.787	0.795	0.792	0.801	0.813	0.807
a (Å)	5.3837	5.303	5.308	5.319	5.324	5.407	5.367
α_{rho} (deg)	60.8596	60.72	60.92	60.83	61.39	61.43	61.66
d(Ni–O) (Å)	1.933	1.896	1.905	1.906	1.923	1.964	1.952
∠Ni–O–Ni (deg)	164.8	167.9	165.6	165.5	163.3	159.6	159.6
θ NiO_6 rotation (deg)	9.2	7.35	8.76	8.19	10.08	12.31	11.17
Ω ($Å^3$/f.u.)	56.2386	53.57	53.97	54.20	55.03	57.71	56.69

TABLE V. Raman-active vibrational modes computed using the various exchange-correlation functionals at the relaxed cell parameters (Table IV) compared to the experimental values.

	E_g	E_g	A_{1g}	E_g	E_g
Experimental	–	156	209	399	451
$U = 0$ eV	72.5	166.4	196.8	374.1	519.4
$U = 3$ eV	73.4	164.0	221.4	388.0	399.4
$U = 6$ eV	66.0	159.6	201.2	330.3	387.3
LSDA-PZ	81.6	171.0	231.5	398.5	509.3
GGA-PBE	84.3	168.9	278.9	351.1	407.1
PBEsol	81.6	169.3	256.3	399.7	458.3

the QE code. To summarize, both the LSDA and the PBEsol functionals predict overall adequate Raman frequencies for LNO that are close to experiment; however, each functional still has deficiencies for specific vibrational modes, and in fact the LSDA values are closest to experiment overall.

We emphasize here that the NiO_6 rotation angle θ, the order parameter characterizing the structural phase transition in $LaNiO_3$, is highly sensitive to the XC functional. Even calculations with the same functional but different pseudopotentials (e.g., the LSDA calculations performed with the VASP and QE codes) yield θ values with obvious differences. Therefore we suggest that an accurate and comprehensive study of various theoretical approximations for the description of octahedra rotation angles in rhombohedral perovskite oxides is needed.

C. Electronic structure and experimental energy spectra

In this section we compare our first-principles results with recent PES data to identify the degree of electronic correlations in rhombohedral $LaNiO_3$. In a single-electron picture, PES measures the excitation energies for noninteracting electrons from the valence band into the continuum and therefore can be used as a first-order reference to single-particle DFT studies. We show in Fig. 7 experimental PES data[27] from a crystalline 20-nm $LaNiO_3$ film and compare it with our first-principles calculated valence band DOS to evaluate the accuracy of our calculations in reproducing the known electronic structure. In order to make a more accurate comparison, we first smear our calculated DOS with a Gaussian function (FWHM = 0.20 eV) to account for the experimental resolution and multiply by a 20 K Fermi-Dirac distribution; we then convolute an energy-dependent Lorentzian function (FWHM $= 0.1|E - E_F|$ eV,[68] where E_F is the Fermi level) with our calculated DOS to include lifetime broadening effects of the photo-excited electrons.

The experimental PES consists of four main features: peaks A and B are assigned to the Ni e_g and t_{2g} states, and the deeper C and D features, to the O $2p$ dominant states.[27] The e_g states (A) are clearly resolved as a sharp peak at the Fermi level, and the strong t_{2g} peak is located at 1.0 eV below the Fermi edge. The O $2p$ states (C), located below the t_{2g} states, correspond to nonbonding O $2p$ states, as their hybridization with the Ni $3d$ states is restricted by symmetry. The O $2p$ bonding states (D) are much broader and located between -8 and -4 eV. Compared to experimental PES results, none of the XC functionals are able to reproduce the sharp spectral

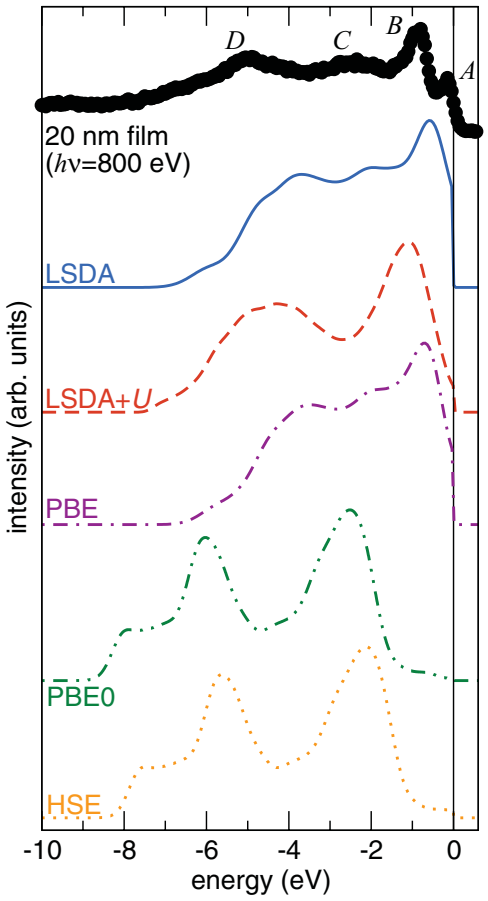

FIG. 7. (Color online) The experimental PES spectrum for a 20-nm crystalline LNO film (filled circles) from Ref. 69 is compared to the density of states calculated with the LSDA + U (U = 5.74 eV), gradient-corrected (PBE) and hybrid (PBE0 and HSE) exchange-correlation functionals. Calculated data are smeared with Lorentzian and Gaussian functions and truncated with a Fermi-Dirac distribution to facilitate the comparison. See the text for peak position assignments.

intensity of the e_g peak at the Fermi level. Each method leads to an overdelocalization of itinerant e_g electrons (Fig. 7).

Despite the inability to reproduce peak A, the LSDA functional does exceedingly well in reproducing the experimental valence band features—both the correct valence bandwidth and the correct energy peak positions. As shown in Fig. 8(a), the LSDA predicts a pronounced hybridization between the Ni t_{2g} and the O $2p$ states almost throughout the full valence band. The e_g states, located at the Fermi level, are separated in energy from the Ni t_{2g} orbitals.

The LSDA + U functional is also able to reproduce the correct bandwidth; however, it fails to predict the correct energy peak positions. It shifts the t_{2g} states (peak B) toward the bonding O $2p$ states (peak D) as observed in the orbital resolved DOS [Fig. 8(b)]. There is an additional shift of bonding O $2p$ spectral weight from the bottom of the valence band to around feature B, which gives the impression that the localized t_{2g} states below the Fermi level are only broadened, and not shifted. These two effects combine to give a reduced intensity in the nonbonding $2p$ states (peak C), whereas experimentally they contribute greater intensity to the PES

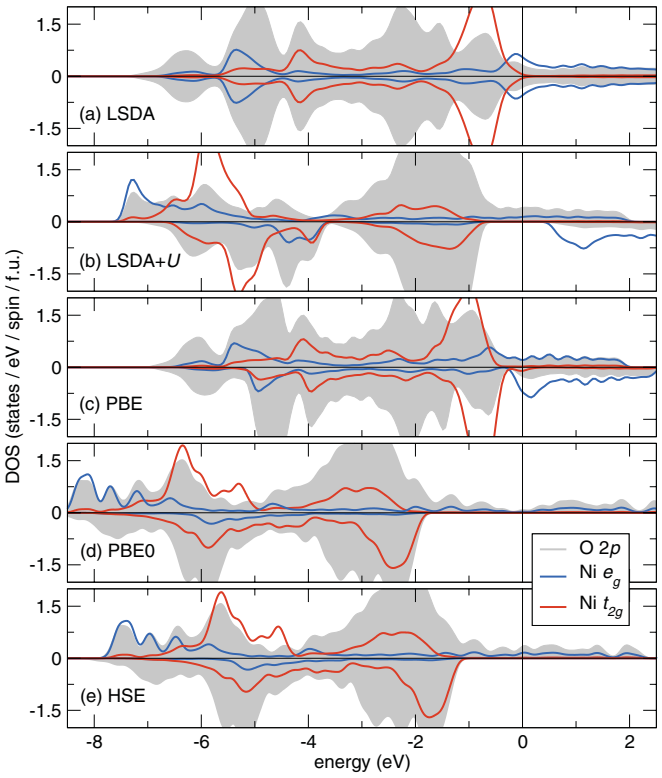

FIG. 8. (Color online) Spin- and orbital-resolved density of states for rhombohedral $LaNiO_3$, obtained from LSDA, LSDA + U (U = 5.74 eV), PBE, PBE0, and HSE calculations. The Fermi energy is the energy 0. In each case the structure is fully relaxed according to the specific functional, with the exception that the DOS for the hybrid XC functionals are calculated with the LSDA ground-state atomic structure.

data. The PBE functional also predicts the correct delocalized electronic character for $LaNiO_3$ but underestimates the valence bandwidth [Fig. 8(c)]. Moreover, it predicts a ferromagnetic ground state (0.56 μ_B local magnetic moment per Ni), in contrast to the paramagnetic LSDA results. Therefore, the PBE functional predicts an electronic structure that is intermediate between the LSDA and the LSDA + U methods.

Both hybrid functionals give poor agreement between the calculated DOS and the experimental PES data. In each case the bandwidth is overestimated, with the PBE0 (HSE) functional ≈1.5 eV (1 eV) larger than the experimental results. This is in contrast to the PBE functional, which produces a narrow (∼6 eV-wide) valence band [Fig. 8(c)]. As mentioned earlier, similar errors are also found in other itinerant magnetic metals when using the PBE0 and HSE functionals.[62] The major peaks are also red-shifted by approximately 2 eV, i.e., the PBE0 and HSE functionals shift the major Ni t_{2g} states to between −7.5 and −5 eV below E_F. Similarly to the LSDA + U approach, the hybrid functionals suppress the contribution of Ni states at E_F. This results in the removal of the Ni e_g states from the Fermi level and shifts them to the bottom of the valence band. This shift of electronic states produces the unusual shoulder at −8 eV in the DOS calculated with the hybrid functionals [Figs. 7(d) and 7(e)].

The above comparison to the experimental data clearly indicates that the beyond-LSDA methods (the LSDA + U and hybrid density functionals) incorrectly describe the electronic structure of $LaNiO_3$. The origin of these discrepancies lies in the fact that the valence band is primarily composed of strongly delocalized Ni t_{2g} and O $2p$ states. Therefore, metallic $LaNiO_3$ is able to strongly screen the electron-electron interactions. This screened electron-electron interaction can lead to renormalization of the electronic states near the Fermi level, which are responsible for the sharp e_g peak observed experimentally.[70] Accurate treatment of this phenomenon in $LaNiO_3$ requires a calculation using many-body DFT methods, i.e., the quasiparticle GW, which includes the dynamically screened Coulomb interaction and therefore treats the electron screening effect in a dynamic (energy-dependent) way.[70] Our beyond-LSDA methods, such as the LSDA + U and hybrid functionals,[57,62] however, are only included in the XC functional, which is independent of the quasiparticle frequency. As such, neither the on-site Coulomb repulsion interaction from the LSDA + U nor the exact-exchange energy from hybrid density functionals is able to reproduce the screening effects (and the above-mentioned discrepancies) present in $LaNiO_3$.

The inability of these beyond-LSDA methods to capture the dynamic screening effects manifests as shifts in core-level binding energies. To explore this effect, we show in Fig. 9 the calculated orbital-resolved DOS in the core energy region (−35 through −10 eV) for $LaNiO_3$. The discrete core-level states are primarily La $5s$ and $5p$ and O $2s$. They are weakly overlapped and easily distinguishable by spectroscopic measurements. In Table VI, we compare our calculated core-level binding energies to recent XPS data.[71] Although the LSDA method accurately reproduces the delocalized states in the valence region, it largely underestimates the binding

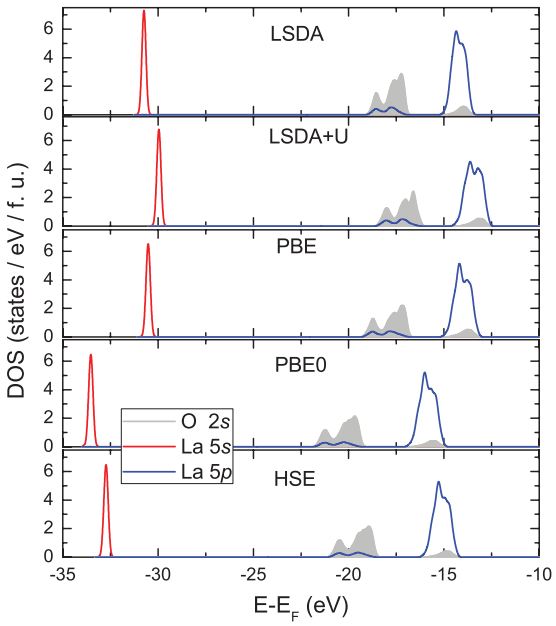

FIG. 9. (Color online) Orbital-resolved density of states in the core energy region obtained from the LSDA, LSDA + U (U = 5.74 eV), PBE, PBE0, and HSE calculations. The Fermi energy level is shifted to the energy 0. Note that the binding energies predicted by the PBE0 and HSE are not obtained by a simple rigid shift of the PBE results.

TABLE VI. Calculated binding energies (in eV) for the major energy peaks in the core region from this study are compared to those calculated with the PBE0 (designated by the *) functional and experimental (Exp.) values, taken from Ref. 71. The assignment of the peak positions follows that of Ref. 71.

Peak	Exp.	LSDA	PBE	LSDA+U	HSE	PBE0	PBE0*
b/c	16.7	14.2	14.4	13.6	15.3	16.0	17.1
d	21.0	17.6	17.6	17.0	19.3	19.8	20.7
e	23.6	18.7	18.6	18.0	20.4	21.1	21.8
f	33.5	30.5	30.7	30.0	32.7	33.5	34.8

energies of the core-level states. In contrast, both hybrid XC functionals significantly improve the description of the peak positions in the core region. Unlike the delocalized valence electrons, the core-level states are weakly modulated by the screening effect from the valence region and, therefore, exhibit strongly localized electronic character. In this case, the hybrid functionals, through the addition of Fock exchange, greatly reduce the self-interaction errors present in the LSDA and GGA functionals and therefore substantially improve the calculated energy spectra. We also note that within the LSDA + U framework, the Hubbard U does not affect the core-level states since it is applied only to the valence Ni 3d orbitals, and therefore the core-level states are only rigidly shifted in energy with respect to those calculated with the LSDA functional.

Based on our first-principles calculations, we find that strong hybridization between the Ni 3d and the O 2p states reduces the on-site d-orbital Coulomb interaction in $LaNiO_3$ through enhanced screening. The conventional LSDA method accurately reproduces the valence band structure and also provides decent experimental agreement with the structural properties. In contrast, the hybrid XC functionals work best for the core-level states. We do find one subtle caveat: the Ni e_g states experimentally exhibit dynamical correlation effects, which we are unable to capture in either the LSDA, the LSDA + U, or the hybrid functionals. This enhanced spectral weight at the Fermi level has recently been reproduced experimentally and through LDA + dynamical mean-field theory calculations,[72–74] where a dynamic (frequency-dependent) treatment of the Ni 3d electron-electron interactions leads to an enhanced effective mass and optical conductivity.

To answer the principal question posed earlier regarding the metallic behavior in $LaNiO_3$: we find that the 3D topology of the perovskite structure with corner-connected NiO_6 octahedra supports strong pd hybridization and stabilizes the metallic state. Moreover, the relatively small octahedral rotations with rhombohedral symmetry and the weak electron-electron correlation effects are insufficient to disrupt the metallic state.

V. SUMMARY AND CONCLUSIONS

In summary, we have studied the lattice normal modes and electronic properties of the correlated metal $LaNiO_3$ with first-principles calculations using a variety of XC functionals. We have examined the rhombohedral-to-cubic structural transition in $LaNiO_3$ within second-order Landau phase transition theory. We found that the A_{1g} Raman-active mode acts as a clear descriptor of the magnitude of the octahedral rotations in rhombohedral perovskites with the $a^-a^-a^-$ tilt pattern. We therefore suggest that Raman spectroscopy is a plausible route for quantifying the magnitude of octahedral rotations in rhombohedral perovskite oxides.

Using a linear response method we have shown that the correlation effects in $LaNiO_3$ originate from the Ni e_g orbitals. We then proposed an orbital-dependent effective Hubbard U value of 5.74 eV for $LaNiO_3$ to be used in the LSDA + U formalism. By comparing the results obtained from the various functionals with experimental spectroscopic data, we found that an accurate treatment of the correlation effects in $LaNiO_3$ cannot be simply obtained by the LSDA + U or hybrid functional methods. We identified that there are strong hybridization effects between the Ni t_{2g} and the O 2p states within $LaNiO_3$ that result in enhanced screening capabilities and act to reduce the electronic correlations in the e_g orbitals. Among the various DFT XC functionals examined, we find that only the LSDA is capable of reproducing *both* the delocalized valence states and the experimentally measured lattice dynamics.

ACKNOWLEDGMENTS

A. M. R. and J. M. R. were supported by the US Office of Naval Research, under grant number N00014-11-1-0664. G. Y. G. was supported by the US Department of Energy, under grant number DE-FG02-07ER46431, and I. G. was supported by the US Office of Naval Research under Grant number N00014-11-1-0578. Computational support was provided by a DURIP grant, a Challenge Grant from the HPCMO, and the high-performance computing facilities at the Argonne Center for Nanoscale Materials. J. M. R. acknowledges travel support from the IMI and AQUIFER Programs of the NSF under Award No. DMR-0843934, managed by the International Center for Materials Research, University of California, Santa Barbara. The authors thank S. J. May, J. E. Spanier, and A. Stroppa for useful discussions.

*gaoyang@sas.upenn.edu
†ilya2@sas.upenn.edu
‡rappe@sas.upenn.edu
§jrondinelli@coe.drexel.edu

[1] M. Stengel, D. Vanderbilt, and N. A. Spaldin, Nat. Mater. **8**, 392 (2009).
[2] N. Sai, A. M. Kolpak, and A. M. Rappe, Phys. Rev. B **72**, 020101 (2005).
[3] A. M. Kolpak, N. Sai, and A. M. Rappe, Phys. Rev. B **74**, 054112 (2006).
[4] W. A. Al-Saidi and A. M. Rappe, Phys. Rev. B **82**, 155304 (2010).

[5]G. Herranz, F. Sánchez, B. Martínez, J. Fontcuberta, M. V. García-Cuenca, C. Ferrater, M. Varela, and P. Levy, Eur. Phys. J. B **40**, 439 (2004).
[6]V. Garcia *et al*., Science **327**, 1106 (2010).
[7]S. Mathews, R. Ramesh, T. Venkatesan, and J. Benedetto, Science **276**, 238 (1997).
[8]K.-T. Kim, C.-I. Kim, J.-G. Kim, and G.-H. Kim, Thin Solid Films **515**, 8082 (2007).
[9]M. Jain, B. S. Kang, and Q. X. Jia, Appl. Phys. Lett. **89**, 242903 (2006).
[10]P. Murugavel, R. Sharma, A. Raju, and C. Rao, J. Phys. D: Appl. Phys. **33**, 906 (2000).
[11]J. L. García-Muñoz, J. Rodríguez-Carvajal, P. Lacorre, and J. B. Torrance, Phys. Rev. B **46**, 4414 (1992).
[12]M. L. Medarde, J. Phys. Condens. Matter **9**, 1679 (1997).
[13]R. Scherwitzl, P. Zubko, C. Lichtensteiger, and J.-M. Triscone, Appl. Phys. Lett. **95**, 222114 (2009).
[14]J. Son, P. Moetakef, J. M. LeBeau, D. Ouellette, L. Balents, S. J. Allen, and S. Stemmer, Appl. Phys. Lett. **96**, 062114 (2010).
[15]R. Scherwitzl, P. Zubko, G. Lezama, S. Ono, A. F. Morpurgo, G. Catalan, and J.-M. Triscone, Adv. Mater. **22**, 5517 (2010).
[16]J. B. Torrance, P. Lacorre, A. I. Nazzal, E. J. Ansaldo, and C. Niedermayer, Phys. Rev. B **45**, 8209 (1992).
[17]P. C. Canfield, J. D. Thompson, S.-W. Cheong, and L. W. Rupp, Phys. Rev. B **47**, 12357 (1993).
[18]X. Obradors, L. M. Paulius, M. B. Maple, J. B. Torrance, A. I. Nazzal, J. Fontcuberta, and X. Granados, Phys. Rev. B **47**, 12353 (1993).
[19]G. Catalan, Phase Transitions **81**, 729 (2008).
[20]M. Imada, A. Fujimori, and Y. Tokura, Rev. Mod. Phys. **70**, 1039 (1998).
[21]J. B. Goodenough and P. M. Raccah, J. Appl. Phys. **36**, 1031 (1965).
[22]K. P. Rajeev, G. V. Shivashankar, and A. K. Raychaudhuri, Solid State Commun. **79**, 591 (1991).
[23]N. Y. Vasanthacharya, P. Ganguly, J. B. Goodenough, and C. N. R. Rao, J. Phys. C **17**, 2745 (1984).
[24]K. Sreedhar, J. M. Honig, M. Darwin, M. McElfresh, P. M. Shand, J. Xu, B. C. Crooker, and J. Spalek, Phys. Rev. B **46**, 6382 (1992).
[25]X. Q. Xu, J. L. Peng, Z. Y. Li, H. L. Ju, and R. L. Greene, Phys. Rev. B **48**, 1112 (1993).
[26]J.-S. Zhou, J. B. Goodenough, B. Dabrowski, P. W. Klamut, and Z. Bukowski, Phys. Rev. Lett. **84**, 526 (2000).
[27]K. Horiba, R. Eguchi, M. Taguchi, A. Chainani, A. Kikkawa, Y. Senba, H. Ohashi, and S. Shin, Phys. Rev. B **76**, 155104 (2007).
[28]J. Tolédano and P. Tolédano, *The Landau Theory of Phase Transitions* (World Scientific, 1987).
[29]J. P. Perdew, M. Ernzerhof, and K. Burke, J. Chem. Phys. **105**, 9982 (1996).
[30]X. Wu, A. Selloni, and R. Car, Phys. Rev. B **79**, 085102 (2009).
[31]J. Heyd, G. E. Scuseria, and M. Ernzerhof, J. Chem. Phys. **118**, 8207 (2003).
[32]J. Heyd, G. E. Scuseria, and M. Ernzerhof, J. Chem. Phys. **124**, 219906 (2006).
[33]J. P. Perdew, K. Burke, and M. Ernzerhof, Phys. Rev. Lett. **77**, 3865 (1996).
[34]V. M. Goldschmidt, Naturwissenschaften **14**, 477 (1926).
[35]A. M. Glazer, Acta Cryst. B **28**, 3384 (1972).
[36]H. T. Stokes, E. H. Kisi, D. M. Hatch, and C. J. Howard, Acta Cryst. B **58**, 934 (2002).
[37]M. V. Abrashev, A. P. Litvinchuk, M. N. Iliev, R. L. Meng, V. N. Popov, V. G. Ivanov, R. A. Chakalov, and C. Thomsen, Phys. Rev. B **59**, 4146 (1999).
[38]R. J. Angel, J. Zhao, and N. L. Ross, Phys. Rev. Lett. **95**, 025503 (2005).
[39]P. Giannozzi *et al*., J. Phys.: Condens. Matter **21**, 395502 (2009), [http://stacks.iop.org/0953-8984/21/395502].
[40]G. Kresse and J. Furthmüller, Phys. Rev. B **54**, 11169 (1996).
[41]G. Kresse and D. Joubert, Phys. Rev. B **59**, 1758 (1999).
[42]J. P. Perdew and A. Zunger, Phys. Rev. B **23**, 5048 (1981).
[43]D. M. Ceperley and B. J. Alder, Phys. Rev. Lett. **45**, 566 (1980).
[44]P. E. Blöchl, Phys. Rev. B **50**, 17953 (1994).
[45]H. J. Monkhorst and J. D. Pack, Phys. Rev. B **13**, 5188 (1976).
[46]X. Gonze and C. Lee, Phys. Rev. B **55**, 10355 (1997).
[47]A. M. Rappe, K. M. Rabe, E. Kaxiras, and J. D. Joannopoulos, Phys. Rev. B **41**, 1227 (1990).
[48]N. J. Ramer and A. M. Rappe, Phys. Rev. B **59**, 12471 (1999).
[49]S. G. Louie, S. Froyen, and M. L. Cohen, Phys. Rev. B **26**, 1738 (1982).
[50]S. Baroni, S. de Gironcoli, and A. D. Corso, Rev. Mod. Phys. **73**, 515 (2001).
[51]X. Gonze, Phys. Rev. A **52**, 1096 (1995).
[52]V. I. Anisimov, F. Aryasetiawan, and A. I. Lichtenstein, J. Phys. Condens. Matter **9**, 767 (1997).
[53]S. L. Dudarev, G. A. Botton, S. Y. Savrasov, C. J. Humphreys, and A. P. Sutton, Phys. Rev. B **57**, 1505 (1998).
[54]M. T. Czyzyk and G. A. Sawatzky, Phys. Rev. B **49**, 14211 (1994).
[55]M. Cococcioni and S. de Gironcoli, Phys. Rev. B **71**, 035105 (2005).
[56]W. E. Pickett, S. C. Erwin, and E. C. Ethridge, Phys. Rev. B **58**, 1201 (1998).
[57]Y. Nohara, S. Yamamoto, and T. Fujiwara, Phys. Rev. B **79**, 195110 (2009).
[58]M. Abbate, G. Zampieri, F. Prado, A. Caneiro, J. M. Gonzalez-Calbet, and M. Vallet-Regi, Phys. Rev. B **65**, 155101 (2002).
[59]X. Wu, E. J. Walter, A. M. Rappe, R. Car, and A. Selloni, Phys. Rev. B **80**, 115201 (2009).
[60]A. Stroppa and S. Picozzi, PhysChemChemPhys **12**, 5405 (2010).
[61]M. Ernzerhof, Chem. Phys. Lett. **263**, 499 (1996).
[62]J. Paier, M. Marsman, K. Hummer, G. Kresse, I. C. Gerber, and J. G. Angyan, J. Chem. Phys. **124**, 154709 (2006).
[63]N. Chaban, M. Weber, S. Pignard, and J. Kreisel, Appl. Phys. Lett. **97**, 031915 (2010).
[64]D. Sarma, N. Shanthi, and P. Mahadevan, J. Phys. Condens. Matter **6**, 10467 (1994).
[65]V. I. Anisimov, D. Bukhvalov, and T. M. Rice, Phys. Rev. B **59**, 7901 (1999).
[66]S. J. May, J.-W. Kim, J. M. Rondinelli, E. Karapetrova, N. A. Spaldin, A. Bhattacharya, and P. J. Ryan, Phys. Rev. B **82**, 014110 (2010).
[67]T. Saha-Dasgupta, Z. S. Popović, and S. Satpathy, Phys. Rev. B **72**, 045143 (2005).
[68]J. J. Sakurai, *Modern quantum mechanics* (Reading, MA: Addison Wesley, Menlo Park, CA, 1985).

[69]Reused with permission from K. Horiba, Phys. Rev. B **76** 155104 (2007). Copyright 2007, The American Physical Society.

[70]R. Eguchi, A. Chainani, M. Taguchi, M. Matsunami, Y. Ishida, K. Horiba, Y. Senba, H. Ohashi, and S. Shin, Phys. Rev. B **79**, 115122 (2009).

[71]Š. Masys, S. Mickevičius, S. Grebinskij, and V. Jonauskas, Phys. Rev. B **82**, 165120 (2010).

[72]M. K. Stewart, C.-H. Yee, J. Liu, M. Kareev, R. K. Smith, B. C. Chapler, M. Varela, P. J. Ryan, K. Haule, J. Chakhalian, D. N. Basov, Phys. Rev. B **83**, 075125 (2011).

[73]P. Hansmann, A. Toschi, X. Yang, O. K. Andersen, and K. Held, Phys. Rev. B **82**, 235123 (2010).

[74]X. Deng, M. Ferrero, J. Mravlje, M. Aichhorn, and A. Georges, e-print arXiv:1107.5920 (2011).